Catalysis Today xxx (xxxx) xxx

Contents lists available at ScienceDirect

Catalysis Today

journal homepage: www.elsevier.com/locate/cattod

Ni-doped A-site excess $SrTiO_3$ thin films modified with Au nanoparticles by a thermodynamically-driven restructuring for plasmonic activity

Kevin G. Both [a], Vilde M. Reinertsen [b], Thomas M. Aarholt [b], Ingvild J.T. Jensen [c], Dragos Neagu [d], Øystein Prytz [b], Truls Norby [a], Athanasios Chatzitakis [a,*]

[a] Centre for Materials Science and Nanotechnology, Department of Chemistry, University of Oslo, Gaustadalléen 21, NO-0349 Oslo, Norway
[b] Centre for Materials Science and Nanotechnology, Department of Physics, University of Oslo, P. O. Box 1048 Blindern, NO-0316 Oslo, Norway
[c] SINTEF Materials Physics, Forskningsveien 1, NO-0373 Oslo, Norway
[d] Department of Chemical and Process Engineering, University of Strathclyde, 75 Montrose St, G1 1XJ Glasgow, United Kingdom

ARTICLE INFO

Keywords:
Metal exsolution
Galvanic replacement
Plasmonic activity
Photocatalysis
Gold
Nanoparticles
Strontium titanate

ABSTRACT

Plasmonically active nanoparticles offer a promising pathway to extend the absorption range of photocatalysts. While not necessarily catalytically active themselves, these particles allow the absorption of lower energy photons in wide band gap photocatalysts. Here, we present A-site excess $SrTiO_3$ thin films, doped with Ni, where through a subsequent exsolution process we created well-socketed Ni nanoparticles in the surface of $SrTiO_3$. These were galvanically replaced by Au, resulting in well-socketed Au nanoparticles with variable size on the surface, depending on the galvanic replacement time. Photoelectrochemical measurements and electron energy loss spectroscopy revealed the improved photoresponse of the thin films by plasmonic activity of the nanoparticles. The energy of the plasmon peak suggests that the main improvement results from the injection of hot charge carriers. Our study opens new avenues for the design and synthesis of the next generation of photocatalytic materials.

1. Introduction

The continued interest in renewable energy sources has led to a plethora of directions to improve the energy harvest efficiency and the energy storage [1–8]. One approach is the utilization of photons to obtain a chemical product by converting the photon energy to chemical energy via a photocatalyst. Photocatalysts are widely investigated for many applications, such as water splitting, environmental remediation, and other uses, each one with specific requirements [2,3,9]. For example, solar water splitting requires a semiconductor with a bandgap of at least 1.23 eV, and taking into account any additional overpotential due to kinetic and thermodynamic losses, this results in an ideal band gap energy of 1.8 – 2.3 eV [2,3,10]. Another key requirement for practical applications is stability, where most stable semiconductors have a bandgap larger than 2.3 eV, ultimately limiting their light absorption capacity, and, consequently, their efficiency [2,3,11]. A promising pathway to enhance the light absorption capacity of a photocatalyst is to combine it with materials exhibiting plasmonic activity. Transfer of photon induced plasmonic energy to the semiconductor can amplify the photoconversion from photonic to chemical energy [12].

The localized surface plasmon resonance (LSPR) is generated on metal nanoparticles (MNPs) on the surface of a semiconductor photocatalyst upon illumination [2]. These MNPs can act as light absorbing antennas or photosensitizers [12], where MNPs and their nanostructures with dimensions significantly smaller than the wavelength of light will have narrow absorption bands in the visible range of the spectrum [13]. The energy of the LSPR can be transferred from the MNP to the semiconductor by three major mechanisms: (i) light scattering/trapping, (ii) plasmon-induced energy transfer (PIRET), and (iii) hot electron injection [8,11]. The effectiveness of the three decay mechanisms for each particle is directly dependent on its size, shape and chemical composition [2,14]. The size distribution, surface states, surface coverage, and surrounding environment of these nanoparticles influence the bandwidth, peak height and position of the absorption maximum [13,15,16], making them ideal for photosensitization of semiconductors [17]. Hence, to predict the results across a macroscopic sample it is imperative to control the size distribution and shape of the particles. The combination of plasmonic MNPs and the semiconductor, forming a

* Corresponding author.
E-mail address: athanasios.chatzitakis@smn.uio.no (A. Chatzitakis).

https://doi.org/10.1016/j.cattod.2022.11.011
Received 29 August 2022; Received in revised form 15 October 2022; Accepted 4 November 2022
Available online 8 November 2022

heterojunction, affects the photoconversion by introducing four different effects: (i) strong light absorption, (ii) intensive far-field light scattering, (iii) abundant hot carrier generation, and (iv) plasmonic heating effects [2,9,12,13,17]. The short lifetime of the excited intra-band transitions remains a challenge for the effective utilization of the plasmonic energy of MNPs [2].

We have recently presented a new synthesis method for supported, well-adhered MNPs [18] and here we extend our method to thin films and A-site excess defective perovskite oxides. We wanted to generalize the concept of exsolution beyond A-site deficient and stoichiometric perovskite by utilizing A-site excess perovskites. A-site excess perovskites typically have Ruddlesden-Popper (RP) interlayers to accommodate the excess A-site ions. In contrast to A-site deficient perovskites there are no inherent A-site vacancies and lower amounts or most likely non-existent oxygen vacancies in the perovskite-like blocks on the RP phase. This creates a host matrix in which metal exsolution is potentially less thermodynamically driven by evolution towards a stoichiometric variant compared to A-site deficient structures [19]. However, A-site excess perovskite might bring kinetic improvements owing to improved ion diffusion in the interlayer region, potentially leading to better control over particle distribution and their socketing depth in the surface of the host semiconductor. Exsolving gold (Au) on A-site excess strontium (STO, $Sr_{1+x}Ti_{1-x}Ni_xO_3$) is considered unfeasible due to the difficulty of dissolving Au in an ionic state in a host perovskite oxide due to the size-coordination preference of Au ions compared to those of typical A or B ions. Meanwhile, the exsolution of nickel (Ni) particles has been studied extensively [20–22], but Ni does not have significant plasmonic activity [14]. However, plasmonically active Au particles can be introduced by a galvanic replacement reaction (GRR) where Ni particles serve as template for Au.

Our method can introduce well-adhered and distributed Au MNPs by galvanically replacing existing MNPs of Ni, formed through exsolution, that are socketed in the surface of the host perovskite material. This electroless process utilizes Ni as the sacrificial template, which is oxidized by a solution containing Au ions. The latter are reduced and deposited on the surface of the template, replacing the original, socketed Ni particles [23–26]. The major advantage is that Au MNPs can by this method be embedded in the perovskite surface, a process that is otherwise very difficult. Partially embedded Au MNPs on glass substrates through a melting procedure have previously been reported to show enhanced stability, while still being able to create charge carriers where they are needed, mainly near the oxide surface, in order to drive chemical reactions [27,28]. We have studied the latter by means of Finite-Difference Time-Domain (FDTD) and our result indicate a strong relation between light absorption efficiency and depth of the socketed Au MNPs in the surface of A-site excess $SrTiO_3$ thin films.

2. Experimental

A pellet of Ni-doped, A-site excess strontium titanate ($Sr_{1.07}Ti_{0.93-}Ni_{0.07}O_{3-\delta}$, STO(Ni)) was prepared by the solid-state reaction method. The appropriate amounts of precursor powders ($SrCO_3$ 99%, (1% Ba) Johnson Matthey GmbH, CAS: 1633–05–2; TiO_2, anatase, Sigma Aldrich, CAS: 1317–70–0; and $Ni(NO_3)_20.6\ H_2O$, 99.999%, Sigma Aldrich, CAS: 13478–00–7) were weighed to obtain 2.5 g of STO(Ni), powder. The precursors were crushed and ball milled in an agate jar with agate balls for 3 h at 300 rpm in de-ionized water (DI H_2O), dried under stirring and subsequently calcined at 450 ℃ for 4 h. The calcined powder was crushed and again ball milled in DI H_2O, dried, pressed to a pellet of 20 mm in diameter, and finally sintered at 1100 ℃ for 12 h.

The pellet was used as target to deposit STO(Ni) films on silicon (Si) wafers by pulsed laser deposition (PLD, Surface-Tec system, laser: Coherent COMPex Pro 205F, KrF, wavelength: 248 nm) at 600 ℃ substrate temperature. The chamber was evacuated, and oxygen gas was used to reach a pressure of 0.005 mbar throughout the process. The target was irradiated with 3.0 J cm^{-2} at a repetition rate of 10 Hz with the distance between the target and substrate being 9 cm. A total of 20,000 shots were applied.

The deposited thin films were then placed in a ProboStat™ sample holder cell (NorECs AS, Norway) in a hydrogen/argon mix (5% H_2, 95% Ar, HArmix) atmosphere. After an initial flushing for 15 min at room temperature, the temperature was raised to 800 ℃, with a ramp rate of 5 ℃ min^{-1} and kept at 800 ℃ for 30 min before it was cooled down to room temperature with 5 ℃ min^{-1}. The described procedure leads to samples with the highest Ni metal signal in XPS (see Fig. S1a). Unless otherwise stated this procedure was followed and the reduced thin films with Ni MNPs will be referred to as STONi.

While the sample was cooling, a solution of 1 mM $HAuCl_4$ in 1 mM HCl was heated to 77 ℃ in a double jacketed beaker connected to a thermostated water bath. The STONi samples were then immediately transferred from the ProboStat™ to the solution, and kept there for 5 s, 30 s and 90 s, thereafter denoted as samples STONiAu5s, STONiAu30s, and STONiAu90s, respectively. Subsequently, each sample was removed for the replacement solution, rinsed with DI H_2O, dried in air, and stored under ambient conditions for analysis.

The analysis consisted of electron microscopy (scanning electron microscopy (SEM) and scanning transmission electron microscopy (STEM), Fei Tecnai-G2 60–300 instrument), including the Energy-Dispersive X-ray Spectroscopy (EDS) and Electron Energy Loss Spectroscopy (EELS), X-ray Photoelectron Spectroscopy (XPS, Kratos Axis Ultra DLD, monochromated A1 Kα), X-ray Diffraction (XRD, Bruker D8 Discover, Cu $K_{\alpha 1}$, Bragg-Brentano), and photoelectrochemical (PEC) measurements (the sample architecture and experimental setup are shown in Fig. S2, while the supplementary note 1 and 2 contains additional details for the STEM, SEM and XPS analyses). PEC measurements were performed with an Ivium Vertex potentiostat/galvanostat in a standard three-electrode set up (Fig. S2a) in 0.5 M Na_2SO_4 (pH = 7.5) as the electrolyte, a saturated calomel electrode (SCE) and a platinum foil as the reference and counter electrodes, respectively. Details for the preparation of the working electrodes can be found in Fig. S2b. All PEC tests were performed under 1 sun simulated solar light, supplied by a Newport Oriel® LCS-100 solar simulator, equipped with a 100 W ozone-free xenon lamp and an AM 1.5 G filter. The light intensity was regularly calibrated by a monocrystalline Si PV reference cell (Newport 91150 V-KG5). All potentials were corrected against the reversible hydrogen electrode (RHE) according to Eq. 1:

$$E_{RHE} = E_{meas.} + 0.059 \times pH + 0.242 \quad V \tag{1}$$

The FDTD calculations were performed in the Ansys Lumerical FDTD Solutions software [29] using the total-field/scattered-field (TFSF) source. A mesh size between 0.2 and 0.8 nm was used, depending on the size and depth of the nanoparticle, in a mesh override region covering the TFSF source region. The number was chosen to be smaller for smaller particles and particles with a smaller depth since these result in geometrical details of small sizes. A non-uniform mesh with a mesh accuracy of 4 was used for the rest of the simulation region, which spanned 1000 nm in every direction. Perfectly matched layers with 8 layers were used as boundary conditions together with two symmetry planes to decrease the computed region. Also, conformal variant 1 was used. The absorption was calculated from a square box of monitors positioned around the MNP, which implies that the absorption includes the STO encapsulated by the box near the MNP surface. Two different permittivity data were used to model both Au [30,31], and Ni [32,33] which are all from Lumerical's Material Database [34] that has the data from CRC Handbook of Chemistry & Physics, Handbook of optical Constants of Solids I – III by E. Palik and Johnson and Christy. Two different permittivity data were also employed for STO; one was extracted from ab initio calculations, i.e., Duan et al. [35] with the help of WebPlotDigitizer [36], and the other was from Dodge [37].

3. Results and Discussion

The structure of the resulting thin films was studied before and after the GRR step by STEM, XRD and SEM. Fig. 1 shows multiple bright field STEM (BF-STEM) images combined with EDS maps, where the Si substrate is at the bottom of each image. In Fig. 1a, a bright field (BF) image overlayed with Ni EDS of STO(Ni) is shown. No columnar growth of the film is seen – the film appears nanocrystalline – and no Ni-rich areas are visible, implying high homogeneity. The XRD measurement of a non-exsolved thin film (Fig. 2a, black line) also shows no distinct peaks beyond the ones attributed to the substrate (Si). Fig. 1(b-e) show the BF overlayed with Ni and Au EDS of STONi, STONiAu90s, STONiAu30s, and STONiAu5s samples, respectively. Here, a columnar structure of the thin film and Ni particles in all the thin films are clearly visible (see also Fig. S3–S5). Au particles are on top, or located in macro-pores, where the Au solution was able to penetrate the thin film during GRR. The longer the galvanic replacement reaction, the larger the Au MNPs were. The diameters of the original Ni particles were less than 25 nm, while the Au MNPs in the studied areas were 10 – 25 nm, 20 – 50 nm and > 40 nm in diameter, for the STONiAu5s, STONiAu30s and STONiAu90s samples, respectively. Moreover, for the longest replacement time the particles took a non-spherical shape (Fig. 1c), yielding multiple absorption peaks in the low-loss spectra of the EELS data, depending on the location of the beam as we will show later. Backscatter electron (BSE), top-view SEM images (Fig. S6) indicate the presence of Au in the STONiAu5s, STONiAu30s and STONiAu90s samples (bright nanoparticles). They also indicate an increase in the MNPs' density and average size from the STONiAu5s to the STONiAu30s, while no significant increase in their density is seen in the STONiAu90s. This agrees well with the shape change of the MNPs in this sample, indicating that most, if not all of the initially exsolved Ni MNPs were replaced by Au already in the STONiAu30s sample and further grown in STONiAu90s.

The XRD patterns in Fig. 2a show the diffraction patterns of the as-deposited, exsolved and galvanically replaced STNOAu5s, STNOAu30s, STNOAu90s thin films. The absence of any peak but the substrate peaks in the non-exsolved sample indicates either a nanocrystalline or amorphous sample. The BF-STEM images in Fig. 1(a-e) confirm that non-exsolved and exsolved samples are different in that the columnar structure appears only in samples exsolved at 800 °C, but not in the non-exsolved specimen (see also Fig. S8–S13). The noticeable exceptions are peaks attributed to the Si substrate, see Fig. S8. All the exsolved patterns show a multitude of peaks, including peaks of $SrTiO_3$ (PDF 01–070–8508), with secondary phases identified as $3SrO{\cdot}SiO_2$ (PDF 00–010–0026), the RP phase Sr_2TiO_4 (PDF 00–039–1471), TiO_2 (PDF 01–070–8501), and naturally the Si substrate (PDF 01–078–6300). The secondary phases may form locally due to favorable interaction with the substrate ($3SrO{\cdot}SiO_2$), or local stoichiometry (Sr_2TiO_4, TiO_2). STO peaks are present and are the most dominant ones after the Si peaks in all the samples. Their relative height and the absence of various peaks from different patterns indicate that the growth of crystal domains is only experiencing a weak templating effect by the substrate. In summary, the XRD and STEM images show exsolution in all thin films, independently of the different crystal orientations and phases present.

In Fig. 2b, the XPS measurements of a STO(Ni) and STONi exsolved in HArmix for 30 min are presented. The XPS results are indicative of the formation of metallic Ni (853 eV) in the reduced sample when compared to the as deposited one, in which no metallic Ni was detected. As expected, the metallic Ni peak is decreasing in intensity (Fig. 2b) while the Au 4f double peak is increasing (Fig. 2c) with increasing immersion times during GRR, in good agreement with the increase in the Au particle size. The Au 4f peaks shift to higher binding energies for increasing Au particle size. The shapes of the peaks are similar and hence do not

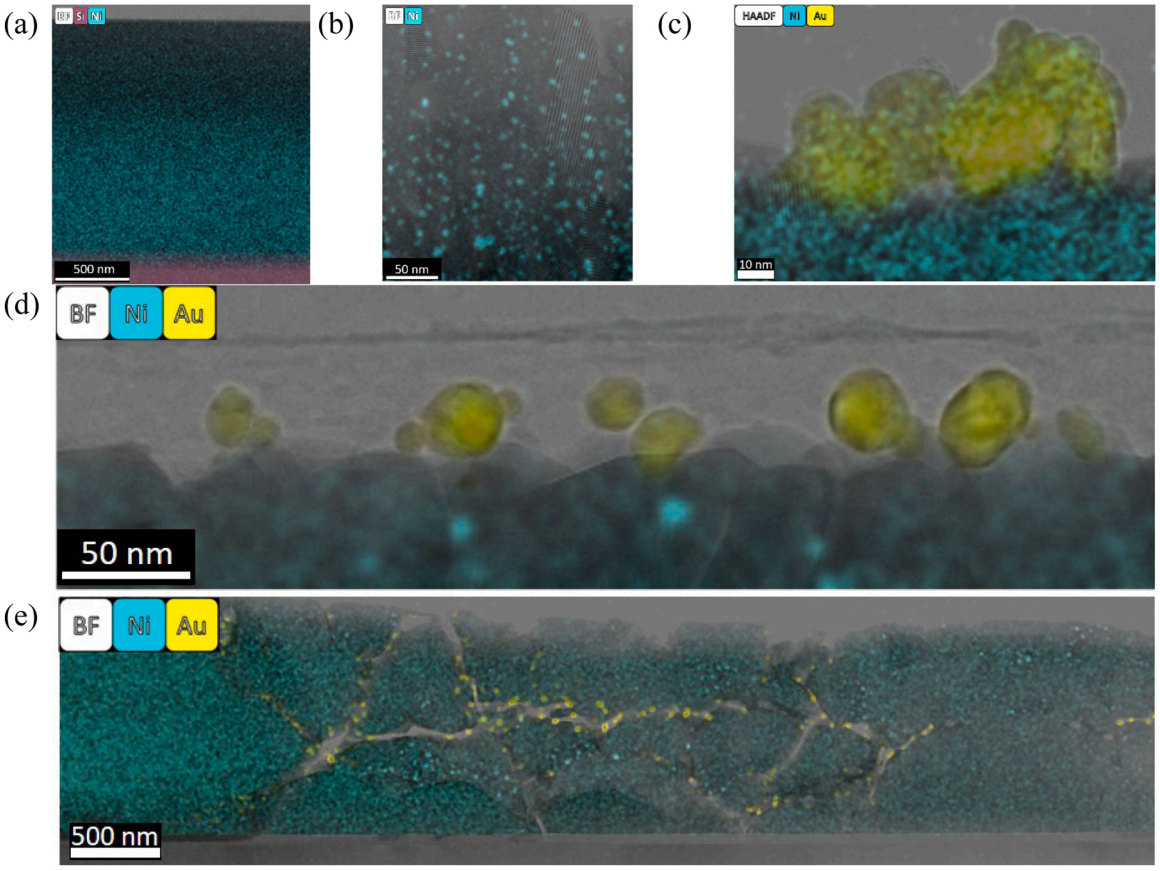

Fig. 1. BF-STEM cross sectional images with overlayed Si, Ni and Au EDS of (a) STO(Ni), (b) STONi, (c) STONiAu90s, (d) STONiAu30s and (e) STONiAu5s. Additional high resolution STEM images of STONiAu5s can be found in Fig. S7 in the SI.

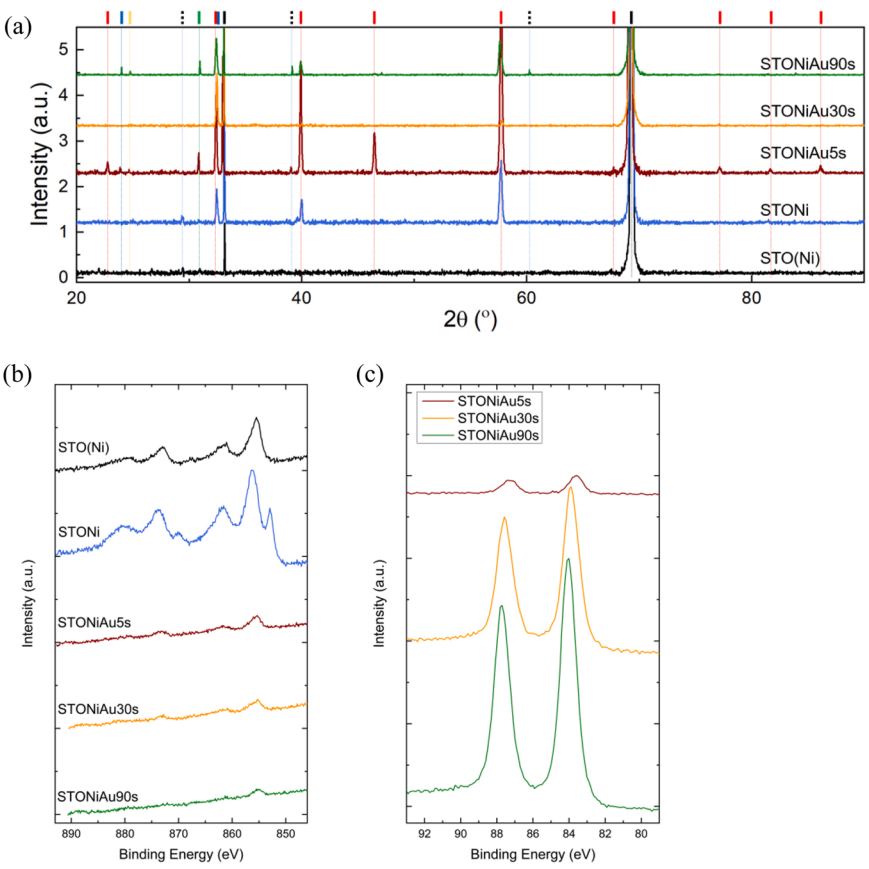

Fig. 2. (a) XRD for the STO(Ni), STONi, STONiAu5s, STONiAu30s, and STONiAu90s. The lines on top mark Si (substrate, black, PDF 01–078–6300), $SrTiO_3$ (red, PDF 01–070–8508), $3SrO{\cdot}SiO_2$ (green, PDF 00–0390–1471), Sr_2TiO_4 (dark blue PDF 00–039–1371), and TiO_2 (yellow, PDF 01–070–8501). Peaks of unknown phases are marked with dotted black lines. (b) XPS spectra of Ni 2p for STO (Ni), STONi, STONiAu5s, STONiAu30s, and STONiAu90s. (c) XPS spectra of Au 4 f of STONiAu5s, STONiAu30s, and STONiAu90s.

suggest that the shift is caused by chemical phase changes. Differential effects of charge compensation on the Au MNPs and the STO substrate could be an explanation (see details of the measurements in supplementary note 2). More work is needed to determine the physical significance of the observed shift in the Au 4f peaks relative to the STO peaks.

The PEC performances of the different samples were studied by linear sweep voltammetry (LSV) in 0.5 M Na_2SO_4 (pH=7.5) and the results are shown in Fig. 3. While the STO(Ni) thin film exhibits a clear generation of photocurrent, as is expected for STO, the photocurrent density of samples with Ni and Au particles varies. For the STNOAu5s sample (Fig. 3c) the photoresponse is hardly noticeable, with the photocurrent being much lower than the STO(Ni). The STNOAu30s sample (Fig. 3a), on the other hand, has a large photocurrent generation. The STNOAu90s sample (Fig. 3d) exhibits prominent recombination spikes, like STO(Ni) (Fig. S14) and STONi (Fig. 3b), indicating a strong charge carrier recombination. While these increased recombination spikes can be an indication of a thermal decay of the plasmons and provide direct evidence of larger PEC capacity, i.e., larger light absorption properties of the plasmonically active samples, their appearance in STO(Ni), STONi and STONiAu90s suggests that they are a property of the deposited film.

The steady state PEC responses at 0.785 V versus RHE (Table S1) of the different samples suggest that the reduction of STO during exsolution decreases the PEC response. The generally low photocurrent densities are attributed to the non-conducting nature of the substrate and the millimeter range that the charge carriers must move in order to reach the Ag contact. The results show that small Au MNPs increase the steady state response compared to the just exsolved sample (Table S1, samples STONi and STONiAu5s), while larger Au MNPs did not have the same effect (Table S1, samples STONi and STONiAu90s). Thus, intermediate Au MNPs size (20–50 nm) as found in the STONiAu30s showed the best performance among all samples, indicating the importance in the size of the plasmonically active MNPs. The higher PEC response suggests that a measurable portion of the photogenerated surface plasmons decay by creating an electron hole pair that can be separated. Chronoamperometric measurements at 0.8 and 1.0 V versus RHE (Fig. S15) are in good agreement with the LSV curves, further showcasing the superiority of the STONiAu30s sample. It is noted that these performances correspond to a duplicate series of these five samples.

To further investigate the size effects of Au MNPs, EELS studies have been performed on individual particles and their surroundings [38]. Fig. 4 and Fig. S16 include particles from STONiAu5s, STONiAu30s, and STONiAu90s. The shape of the particles can be seen in the STEM images. EELS maps with selected energy ranges are shown in the EELS map column. The energy ranges are 1.505–1.520 eV for the STONiAu90s, 2.35–2.40 eV for the STONiAu30s and STONiAu5s. They were selected based on the most dominant peak in the given map. EELS spectra of selected pixels, indicated with colored frames in the maps are presented in the EELS graph column. These graphs reiterate that the peak around 1.5 eV dominates the spectra for the STONiAu90s sample, with minor peaks between 1.9 eV and 2.4 eV. On the other hand, for the STONiAu30s and STONiAu5s samples, which showed improved PEC activity the spectra exhibit one peak at 2.4 eV, which is the expected peak for the plasmonic activity of Au MNPs [14].

The position of the peaks in all samples suggest that the major mechanism for charge carrier transfer between the plasmonically active MNPs and the STO is hot charge carrier transfer. The spectral overlap between Au MNPs and STO determines the PIRET response [2], which is very limited as our calculations indicate in Fig. S17, while scattering/-trapping would only increase the chances of exciting an electron-hole pair by photons with an energy larger than the band gap of STO. Additionally, the positions of the EELS peaks in all samples suggest that the major mechanism by which the plasmonic energy is utilized is either

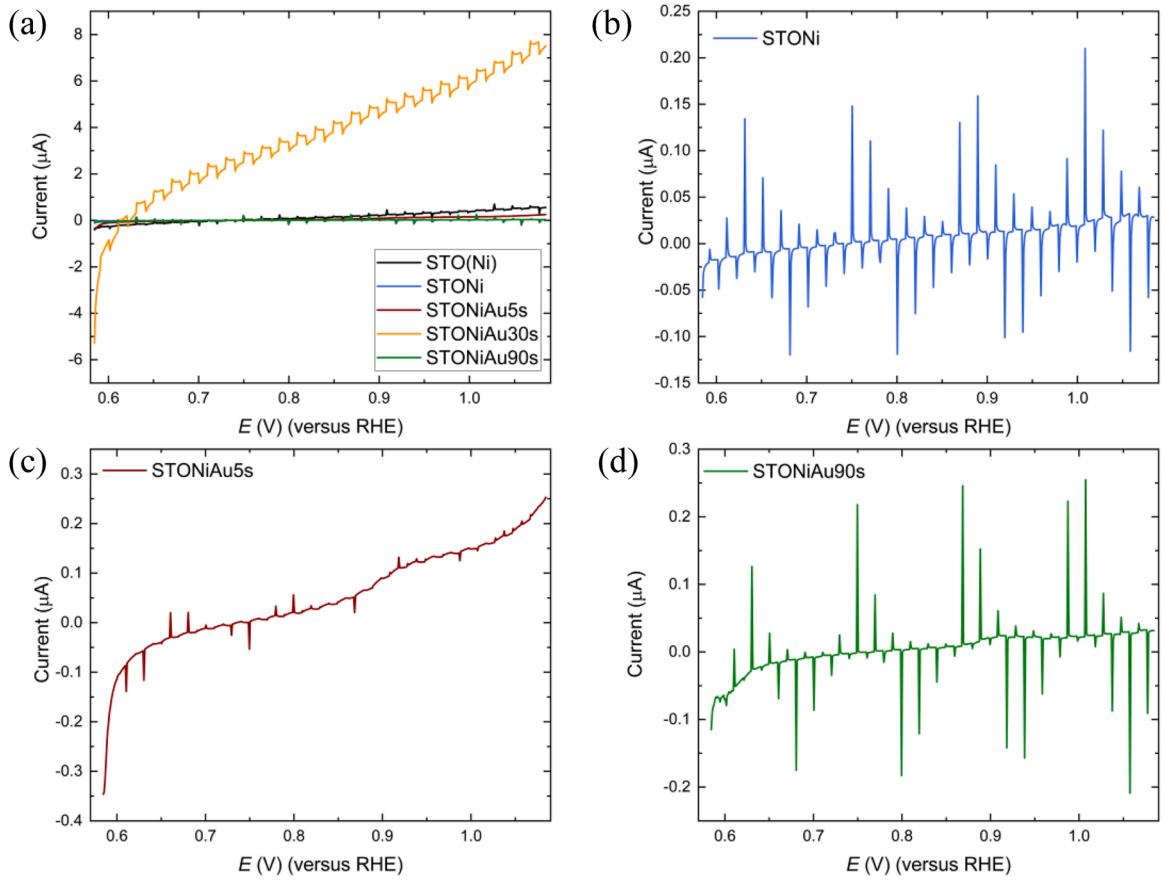

Fig. 3. (a) LSV curves of all samples under chopped illumination conditions in 0.5 M Na_2SO_4. LSVs from (a) but at narrower potentials for (b) STONi, (c) STONiAu5s, and (d) STONiAu90s. Scan rate 5 mV s^{-1}.

local heating or hot charge carrier transfer between the plasmonically active MNPs and the STO. The hot charge carrier transfer is then suggested as the main mechanism for energy transfer between the plasmonic MNPs and STO, although a combination of hot charge carriers and local heating cannot be conclusively excluded.

4. Calculations

Computational studies in the form of FDTD calculations [29] of Au and Ni MNPs with randomly selected diameters between 10 nm and 30 nm were performed to study the effect of embedding the MNPs. In these calculations, the centers of the spheres were placed at different depths compared to the surface of STO (Fig. 5a). The study revealed two important findings: First, Au particles showed enhanced absorption in comparison to Ni particles located at the same depth (Fig. 5b). Second, particles with their center buried in STO have increased absorption compared to the particles with their center at or above the STO surface (Fig. 5c, and total absorptions given in Fig. S18). We believe the increased absorption is due to a red-shift of the peak (Fig. S19), bringing it away from interband transitions (at 2.4 eV [14]) that lead to damping. Consequently, we predict that partially buried particles as a result of exsolution and GRR, show an enhanced absorption cross section compared to deposited particles (physical deposition, photodeposition and other such methods). Moreover, we also calculated absorption cross sections of deposited particles compared to embedded particles, i.e. 'dome particles (Fig. 5b). Dome particles were defined as spherical MNPs with a flat interface with STO (Fig. 5a). Here, the depth refers to the position of the flat interface and the results show that the absorption is similar for the dome particles and the spherical particles (particles with 0% in Fig. 5a). Finally, burying a particle deeper inside the surface also increases the interface area between the MNP and the STO, which has been shown to increase the probability of hot charge carrier injection [39]. Metal exsolution is an appropriate method for controlling the socketing depth of a particle and control over this process will be of great importance for the design of highly efficient, plasmonically active photocatalysts.

5. Conclusions

Our methodology enables the formation of well-socketed Au MNPs of various sizes and shapes created by galvanic replacement of exsolved Ni by Au ions on A-site excess STO thin films. We demonstrated that the shape and size of the particles lead to differences in EELS mapping. Specifically, large non-spherical particles as observed in sample STONiAu90s exhibit multiple peaks that ultimately decrease the PEC activity, while spherical particles as in STONiAu5s and STONiAu30s have a singular peak around 2.4 eV, and improved PEC activity. This suggests that an intermediate size distribution of Au MNPs allows the dominant energy transfer mechanism from MNP to STO that is found to occur through hot charge carrier transfer. Our FDTD calculations highlighted that embedded particles can heavily improve the absorption cross section, more than particles on the surface of the photocatalyst, reflecting the need to create well-socketed, plasmonically active particles not only to improve their stability, but also their plasmonic response. This is now possible through our method of metal exsolution and galvanic replacement and efforts to gain control over particles' socketing depth, size and distribution will open the way for the next generation of photocatalytic materials.

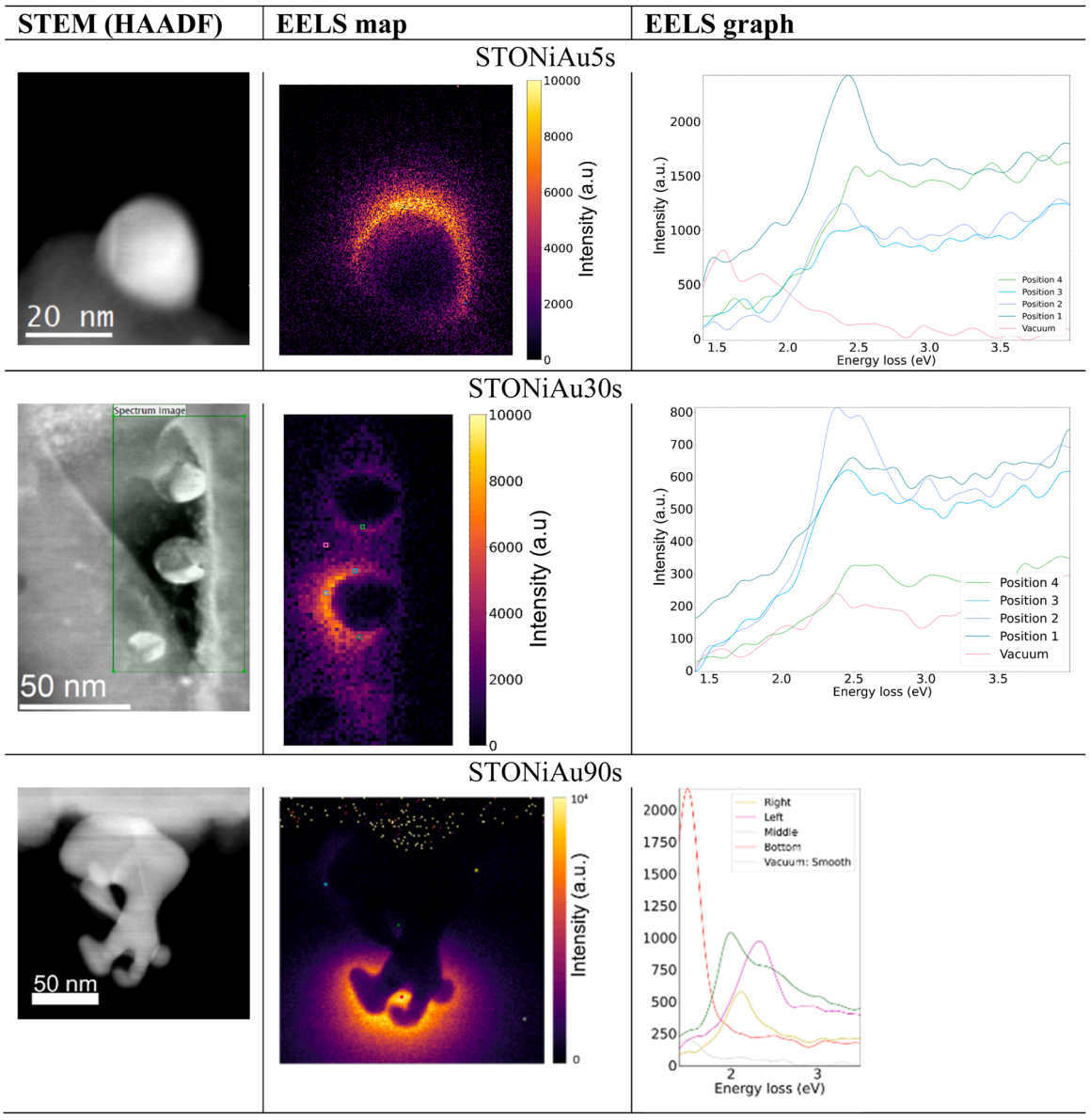

Fig. 4. STEM HAADF images of Au particles on STONiAu5s, STONiAu30s, and STONiAu90s samples, with the corresponding EELS map and EEL spectra from the selected pixels in each image.

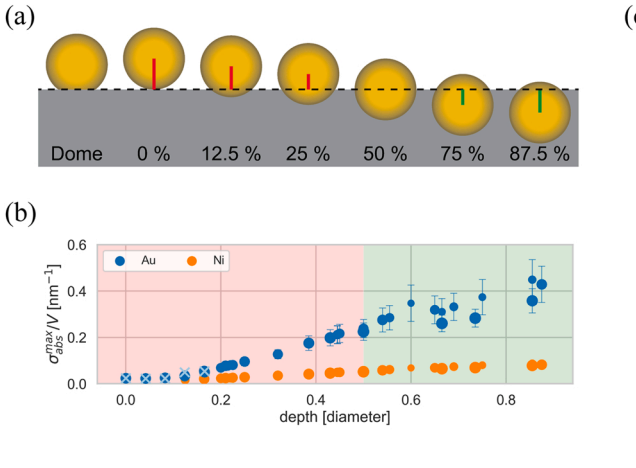

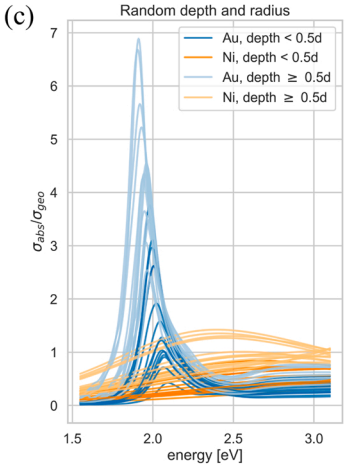

Fig. 5. (a) Illustration of the sphere placements for the calculations. (b) Absorption cross sections normalized with the geometrical cross section for Ni and Au particles on STO located at different depths. (c) Maximum absorption cross section per volume against the depth of the particle both for Ni and Au. The marker-size reflects the size of the nanoparticle in the particular simulation. Additional calculations of dome-type Au particles are shown as light blue crosses. The error bars show the spread of the peak height with different permittivity data for the metal and STO (see also Fig. S20). The spread is so small for Ni that the error bars are smaller than the marker.

CRediT authorship contribution statement

Kevin G. Both: Methodology, Validation, Formal analysis, Investigation, Visualization, Writing – original draft, Review and editing **Vilde M. Reinertsen:** Methodology, Validation, Formal analysis, Investigation, Visualization, Writing – review and editing **Thomas M. Aarholt:** Investigation, Formal analysis, Writing – review and editing **Ingvild J. T. Jensen:** Investigation, Writing – review and editing. **Dragos Neagu:** Methodology, Writing – review and editing **Øystein Prytz:** Resources, Writing – review and editing, Supervision **Truls Norby:** Resources, Writing – review and editing, Supervision. **Athanasios Chatzitakis:** Conceptualization, Methodology, Investigation, Writing – original draft, Review and editing, Visualization, Supervision, Project administration, Funding acquisition.

Declaration of Competing Interest

The authors declare that they have no known competing financial interests or personal relationships that could have appeared to influence the work reported in this paper.

Data availability

Data will be made available on request.

Acknowledgements

The Research Council of Norway is acknowledged for the support to the Norwegian Center for Transmission Electron Microscopy (NORTEM, no. 197405/F50), the NANO2021 researcher project FUNCTION (no. 287729) and FRINATEK project PH2ON (no. 288320).

Appendix A. Supporting information

Supplementary data associated with this article can be found in the online version at doi:10.1016/j.cattod.2022.11.011.

References

[1] D. Ravelli, D. Dondi, M. Fagnoni, A. Albini, Photocatalysis. A multi-faceted concept for green chemistry, Chem. Soc. Rev. 38 (2009) 1999–2011, https://doi.org/10.1039/B714786B.
[2] N. Wu, Plasmonic metal–semiconductor photocatalysts and photoelectrochemical cells: a review, Nanoscale 10 (2018) 2679–2696, https://doi.org/10.1039/C7NR08487K.
[3] M.G. Walter, E.L. Warren, J.R. McKone, S.W. Boettcher, Q. Mi, E.A. Santori, N. S. Lewis, Solar water splitting cells, Chem. Rev. 110 (2010) 6446–6473, https://doi.org/10.1021/cr1002326.
[4] G.L. Soloveichik, Battery technologies for large-scale stationary energy storage, Annu. Rev. Chem. Biomol. Eng. 2 (2011) 503–527, https://doi.org/10.1146/annurev-chembioeng-061010-114116.
[5] E. Kabir, P. Kumar, S. Kumar, A.A. Adelodun, K.-H. Kim, Solar energy: potential and future prospects, Renew. Sustain. Energy Rev. 82 (2018) 894–900, https://doi.org/10.1016/j.rser.2017.09.094.
[6] D.J. Willis, C. Niezrecki, D. Kuchma, E. Hines, S.R. Arwade, R.J. Barthelmie, M. DiPaola, P.J. Drane, C.J. Hansen, M. Inalpolat, J.H. Mack, A.T. Myers, M. Rotea, Wind energy research: State-of-the-art and future research directions, Renew. Energy 125 (2018) 133–154, https://doi.org/10.1016/j.renene.2018.02.049.
[7] H. Andersen, K. Xu, D. Malyshkin, R. Strandbakke, A. Chatzitakis, A highly efficient electrocatalyst based on double perovskite cobaltites with immense intrinsic catalytic activity for water oxidation, Chem. Commun. 56 (2020) 1030–1033, https://doi.org/10.1039/C9CC08765F.
[8] M.M. Momeni, Y. Ghayeb, N. Moosavi, Preparation of Ni–Pt/Fe–TiO2 nanotube films for photoelectrochemical cathodic protection of 403 stainless steel, Nanotechnology 29 (2018), 425701.
[9] Q. Zhang, D.T. Gangadharan, Y. Liu, Z. Xu, M. Chaker, D. Ma, Recent advancements in plasmon-enhanced visible light-driven water splitting, J. Mater. 3 (2017) 33–50, https://doi.org/10.1016/j.jmat.2016.11.005.
[10] M. Volokh, G. Peng, J. Barrio, M. Shalom, Carbon nitride materials for water splitting photoelectrochemical cells, Angew. Chem. Int. Ed. 58 (2019) 6138–6151, https://doi.org/10.1002/anie.201806514.
[11] M. Ben-Naim, R.J. Britto, C.W. Aldridge, R. Mow, M.A. Steiner, A.C. Nielander, L. A. King, D.J. Friedman, T.G. Deutsch, J.L. Young, T.F. Jaramillo, Addressing the Stability Gap in Photoelectrochemistry: Molybdenum Disulfide Protective Catalysts for Tandem III–V Unassisted Solar Water Splitting, ACS Energy Lett. 5 (2020) 2631–2640, https://doi.org/10.1021/acsenergylett.0c01132.
[12] J. Li, Z. Lou, B. Li, Engineering plasmonic semiconductors for enhanced photocatalysis, J. Mater. Chem. A 9 (2021) 18818–18835, https://doi.org/10.1039/D1TA04541E.
[13] E. Hutter, J.H. Fendler, Exploitation of localized surface plasmon resonance, Adv. Mater. 16 (2004) 1685–1706, https://doi.org/10.1002/adma.200400271.
[14] U. Kreibig, M. Vollmer, Optical Properties of Metal Clusters, Springer Berlin Heidelberg, 2013. ⟨https://books.google.no/books?id=6WrrCAAAQBAJ⟩.
[15] S. Underwood, P. Mulvaney, Effect of the solution refractive index on the color of gold colloids, Langmuir 10 (1994) 3427–3430, https://doi.org/10.1021/la00022a011.
[16] M.E. Stewart, C.R. Anderton, L.B. Thompson, J. Maria, S.K. Gray, J.A. Rogers, R. G. Nuzzo, Nanostructured Plasmonic Sensors, Chem. Rev. 108 (2008) 494–521, https://doi.org/10.1021/cr068126n.
[17] M.M. Abouelela, G. Kawamura, A. Matsuda, A review on plasmonic nanoparticle-semiconductor photocatalysts for water splitting, J. Clean. Prod. 294 (2021), 126200, https://doi.org/10.1016/j.jclepro.2021.126200.
[18] X. Kang, V.M. Reinertsen, K.G. Both, A. Galeckas, T. Aarholt, Ø. Prytz, T. Norby, D. Neagu, A. Chatzitakis, Galvanic Restructuring of Exsolved Nanoparticles for Plasmonic and Electrocatalytic Energy Conversion, Small. N./a (2022), 2201106, https://doi.org/10.1002/smll.202201106.
[19] G. Tsekouras, D. Neagu, J.T.S. Irvine, Step-change in high temperature steam electrolysis performance of perovskite oxide cathodes with exsolution of B-site dopants, Energy Environ. Sci. 6 (2013) 256–266, https://doi.org/10.1039/C2EE22547F.
[20] F.N. Agüero, A.M. Beltrán, M.A. Fernández, L.E. Cadús, Surface nickel particles generated by exsolution from a perovskite structure, J. Solid State Chem. 273 (2019) 75–80, https://doi.org/10.1016/j.jssc.2019.02.036.
[21] D. Neagu, T.-S. Oh, D.N. Miller, H. Ménard, S.M. Bukhari, S.R. Gamble, R.J. Gorte, J.M. Vohs, J.T.S. Irvine, Nano-socketed nickel particles with enhanced coking resistance grown in situ by redox exsolution, Nat. Commun. 6 (2015) 8120, https://doi.org/10.1038/ncomms9120.
[22] T.-S. Oh, E.K. Rahani, D. Neagu, J.T.S. Irvine, V.B. Shenoy, R.J. Gorte, J.M. Vohs, Evidence and Model for Strain-Driven Release of Metal Nanocatalysts from Perovskites during Exsolution, J. Phys. Chem. Lett. 6 (2015) 5106–5110, https://doi.org/10.1021/acs.jpclett.5b02292.
[23] X. Xia, Y. Wang, A. Ruditskiy, Y. Xia, 25th Anniversary article: galvanic replacement: a simple and versatile route to hollow nanostructures with tunable and well-controlled properties, Adv. Mater. 25 (2013) 6313–6333, https://doi.org/10.1002/adma.201302820.
[24] S.E. Skrabalak, J. Chen, Y. Sun, X. Lu, L. Au, C.M. Cobley, Y. Xia, Gold nanocages: synthesis, properties, and applications, Acc. Chem. Res. 41 (2008) 1587–1595, https://doi.org/10.1021/ar800018v.
[25] C.M. Cobley, Y. Xia, Engineering the properties of metal nanostructures via galvanic replacement reactions, Mater. Sci. Eng. R. Rep. 70 (2010) 44–62, https://doi.org/10.1016/j.mser.2010.06.002.
[26] Y. Sun, B.T. Mayers, Y. Xia, Template-engaged replacement reaction: a one-step approach to the large-scale synthesis of metal nanostructures with hollow interiors, Nano Lett. 2 (2002) 481–485, https://doi.org/10.1021/nl025531v.
[27] S. Zhu, D. Wang, Photocatalysis: basic principles, diverse forms of implementations and emerging scientific opportunities, Adv. Energy Mater. 7 (2017), 1700841, https://doi.org/10.1002/aenm.201700841.
[28] R.S. Moirangthem, M.T. Yaseen, P.-K. Wei, J.-Y. Cheng, Y.-C. Chang, Enhanced localized plasmonic detections using partially-embedded gold nanoparticles and ellipsometric measurements, Biomed. Opt. Express 3 (2012) 899–910, https://doi.org/10.1364/BOE.3.000899.
[29] ⟨https://www.lumerical.com/⟩, n.d. https://www.lumerical.com/.
[30] C.G. Olson, D.W. Lynch, J.H. Weaver, (n.d.). unpublished.
[31] P.B. Johnson, R.W. Christy, Optical Constants of the Noble Metals, Phys. Rev. B 6 (1972) 4370–4379, https://doi.org/10.1103/PhysRevB.6.4370.
[32] D.W. Lynch, R. Rosei, J.H. Weaver, Infrared and visible optical properties of single crystal Ni at 4K, Solid State Commun. 9 (1971) 2195–2199, https://doi.org/10.1016/0038-1098(71)90629-6.
[33] E.D. Palik, Handbook of optical constants of solids, Academic press,, 1998.
[34] Material Database in FDTD and MODE, (n.d.). ⟨https://support.lumerical.com/hc/en-us/articles/360034394614-Material-Database-in-FDTD-and-MODE⟩.
[35] Y. Duan, P. Ohodnicki, B. Chorpening, G. Hackett, Electronic structural, optical and phonon lattice dynamical properties of pure- and La-doped SrTiO3: An ab initio thermodynamics study, J. Solid State Chem. 256 (2017) 239–251, https://doi.org/10.1016/j.jssc.2017.09.016.
[36] A. Rohatgi, WebPlotDigitizer, 2020. ⟨https://automeris.io/WebPlotDigitizer⟩.
[37] M.J. Dodge, Refractive Index, McGraw-Hill 2009), in: M.J. Weber (Ed.), 3rd edition.,Handbook of Laser Science and Technology, Volume IV, Optical Material: Part 2, (as cited in Handbook of Optics, Vol. 4, CRC Press, Boca Raton, 1986.
[38] R.F. Egerton, Scattering delocalization and radiation damage in STEM-EELS, Ondrej Krivanek Res, Life EELS Aberration Corrected STEM 180 (2017) 115–124, https://doi.org/10.1016/j.ultramic.2017.02.007.
[39] X.-C. Ma, Y. Dai, L. Yu, B.-B. Huang, Energy transfer in plasmonic photocatalytic composites, Light Sci. Appl. 5 (2016) e16017–e16017.